AAAS
Research
Volume 2020, Article ID 1672051, 12 pages
https://doi.org/10.34133/2020/1672051

*Research Article*

# The Electronic Transport Channel Protection and Tuning in Real Space to Boost the Thermoelectric Performance of $Mg_{3+\delta}Sb_{2-y}Bi_y$ near Room Temperature

**Zhijia Han,[1,2] Zhigang Gui,[3,4] Y. B. Zhu,[1] Peng Qin,[1] Bo-Ping Zhang,[2] Wenqing Zhang,[3] Li Huang,[3] and Weishu Liu[1,5]**

[1]*Department of Materials Science and Engineering, Southern University of Science and Technology, Shenzhen 518055, China*
[2]*School of Materials Science and Engineering, University of Science and Technology Beijing, Beijing 10083, China*
[3]*Department of Physics, Southern University of Science and Technology, Shenzhen 518055, China*
[4]*Academy for Advanced Interdisciplinary Studies, Southern University of Science and Technology, Shenzhen 518055, China*
[5]*Shenzhen Engineering Research Center for Novel Electronic Information Materials and Devices, Southern University of Science and Technology, Shenzhen 518055, China*

Correspondence should be addressed to Li Huang; huangl@sustech.edu.cn and Weishu Liu; liuws@sustech.edu.cn

Received 20 December 2019; Accepted 12 February 2020; Published 28 February 2020



The optimization of thermoelectric materials involves the decoupling of the transport of electrons and phonons. In this work, an increased $Mg_1$-$Mg_2$ distance, together with the carrier conduction network protection, has been shown as an effective strategy to increase the weighted mobility ($U = \mu m^{*3/2}$) and hence thermoelectric power factor of $Mg_{3+\delta}Sb_{2-y}Bi_y$ family near room temperature. $Mg_{3+\delta}Sb_{0.5}Bi_{1.5}$ has a high carrier mobility of 247 $cm^2 V^{-1} s^{-1}$ and a record power factor of 3470 $\mu W m^{-1} K^{-2}$ at room temperature. Considering both efficiency and power density, $Mg_{3+\delta}Sb_{1.0}Bi_{1.0}$ with a high average ZT of 1.13 and an average power factor of 3184 $\mu W m^{-1} K^{-2}$ in the temperature range of 50-250°C would be a strong candidate to replace the conventional n-type thermoelectric material $Bi_2Te_{2.7}Se_{0.3}$. The protection of the transport channel through Mg sublattice means alloying on Sb sublattice has little effect on electron while it significantly reduces phonon thermal conductivity, providing us an approach to decouple electron and phonon transport for better thermoelectric materials.

## 1. Introduction

Thermoelectric (TE) materials offer the convenience to convert the widely distributed waste heat into electric power directly, which is highly desired for the autonomous operation of the Internet of things (IoT) in recent years. The conventional room temperature (RT) thermoelectric material, $Bi_2Te_3$ family, dominates the market of the solid-state refrigeration [1, 2]. However, its mediocre mechanical property and the extremely low abundance of Te element limit its application [3]. The past years have witnessed great progress in developing medium-temperature thermoelectric materials, but not so much in near room temperature TE materials. So far, there is no candidate material that can compete with the $Bi_2(Te,Se)_3$ family in terms of near room temperature TE performance. In our previous report, we have shown that the Mn-doped $Mg_{3+\delta}Sb_{1.5}Bi_{0.5}$ ($(ZT)_{avg} = 1.05$, $K_{IC} = 2.2\text{-}3.0$ MPa $m^{1/2}$) would be a very promising candidate for substituting the $Bi_2Te_{3-x}Se_x$ family ($(ZT)_{avg} = 0.9 - 1.0$, $K_{IC} = 0.6\text{-}1.3$ MPa $m^{1/2}$) in the temperature range of 50–250°C because of the comparable average ZT and much higher fracture toughness [4]. It is noted that intensive efforts have been made into searching high ZT composition in the Bi-rich $Mg_{3+\delta}Sb_{2-y}Bi_y$ with varying doping [5–7]. Imasato et al. researched Bi content-dependent thermoelectric properties and discovered that $Mg_{3+\delta}Sb_{0.6}Bi_{1.4}$ shows exceptional thermoelectric performance [8]. Ren et al. produced a thermoelectric cooling couple with $Mg_{3+\delta}Sb_{0.5}Bi_{1.5}$ and $Bi_{0.5}Sb_{1.5}Te_3$, which realized $\Delta T$ around 90 K at the hot-side $T$ of 350 K. Further improvement on the power factor is desirable for power generation applications [9]. However, the power factor of the reported

$Mg_{3+\delta}Sb_{1.5}Bi_{0.5}$ is still lower than that of the $Bi_2Te_{3-x}Se_x$ family, which could lead to a reduced power density of the thermoelectric power generator. Further enhancement in the PF of $Mg_{3+\delta}Sb_{1.5}Bi_{0.5}$ is thus much desired.

However, it is challenging to decouple the transport of electrons while tuning the thermoelectric properties [10]. Electron-phonon interaction and defects would affect electron and phonon transport at the same time. The material parameter $B$ ($B \propto \mu m^{*3/2}/\kappa_{lat}$) is commonly used as a guideline to boost thermoelectric performance of materials, where $\mu$ and $m^*$ are the carrier mobility and effective mass, respectively [11]. Usually, a material that has multicarrier valleys and small DOS effective mass for each valley could have a large power factor ($S^2\sigma$) [12], and a material with heavy elements can have low intrinsic $\kappa$ [13]. For instance, $Bi_2Te_3$ and PbTe are known as conventional thermoelectric materials. Also, alloying has been greatly used to reduce the lattice thermal conductivity after Ioffe's [14] and Goldsmid's [15] pioneering works. However, the decrease in $\kappa$ from alloying is usually offset by the reduction in $\mu$ from alloying [16]. Recently, Liu et al. have found that the small atomic size difference between the period 5 elements (Zr, Nb) and period 6 elements (Hf, Ta) moderates alloying's negative impact on carrier mobility in the half-Heusler system [17].

In 2016, Tamaki et al. reported an n-type $Mg_{3+\delta}Sb_2$-based laminar Zintl compound with a high ZT of 1.5 at 442°C [18], which has attracted much attention in the thermoelectric community to enhance the peak ZT of $Mg_{3+\delta}Sb_2$-based TE materials [19–22]. The most surprising feature of this material family is that the alloy disorder at anionic sites has little effect on carrier mobility. Favorable alloying sites are known in the $Bi_2Te_3$ family, i.e., n-type $Bi_2Te_3$ has a favorable site at the Te sublattice while the p-type one has a favorable site at the Bi sublattice. Similar favorable doping sites have been observed in the PbTe [23, 24] and $Mg_2Sn$ [25] systems. Wang et al. suggested that the favorable dopants should be on the site that is of less influence on the charge-conducting band [24]. Recently, Yang et al. proposed a conduction network in the real space: the vast majority of atoms formed a conductive framework for charge carriers, while the chief role of the remaining atoms was to scatter phonons [26]. If the alloying elements or dopants get into the sublattice away from the conduction network, they would have little impact on carriers' transport. Tamaki et al. also pointed out the conduction network, formed by the 3s-like orbitals of $Mg^{2+}$ and the weakly hybridized atomic orbitals of $[Mg_2Sb_2]^{2-}$ in $Mg_{3+\delta}Sb_2$-based layered Zintl compound, but not connecting with the feature that alloying has little effect on carrier mobility. We believe that this carrier conductive network forms a favorable carrier transport channel in real space. It was found that the disordering Bi/Sb at the anionic site is "far away" from the electronic transport channel, which explains the fact that the electrical conductivity of $Mg_{3+\delta}Sb_{1.5}Bi_{0.5}$ is very sensitive to the Mg vacancy but not to the disordering Bi/Sb [18, 27, 28]. Experimentally, excess Mg is necessary to suppress the formation of Mg vacancy and obtain stable n-type samples [19]. However, as suggested by Tamaki et al., Mg vacancy is still a favorable intrinsic defect even in a Mg-rich condition. In our previous work [4], we have shown that the Mn dopant at $Mg_4$-tetrahedron interstitial site provides an attracting force to suppress the formation of the Mg vacancy.

In this work, we will theoretically show a more unique character of the carrier conduction network: by increasing the $Mg_1$-$Mg_2$ distance, we can increase the weighted mobility $U$ and enhance the power factor ($S^2\sigma$) through the increased carrier mobility. Experimentally, we found the Bi-rich $Mg_{3+\delta}Sb_{2-y}Bi_y$ with interstitial dopant Mn and anionic dopant Te has a recorded high carrier mobility of $247\,cm^2\,V^{-1}\,s^{-1}$ and a high power factor of $3470\,\mu W\,m^{-1}\,K^{-2}$ at room temperature in the $Mg_{3+\delta}Sb_{0.5}Bi_{1.5}$ sample. The $Mg_{3+\delta}Sb_{1.0}Bi_{1.0}$ possessed a high average ZT of 1.13 and an average PF of $3184\,\mu W\,m^{-1}\,K^{-2}$ in the temperature range of 50-250°C.

## 2. Results and Discussion

Figure 1 shows the effect of increased $Mg_1$-$Mg_2$ distance in real space on the band structure and Hall mobility. Our motivation was to find a way to further tailor the charge conductive network in real space and make it more favorable for the transport of electrons. $Mg_3Sb_2$ has a trigonal structure (space group: $P\bar{3}m1$) and a layered structure with alternate layers of Mg and $[Mg_2Sb_2]$ in the ab-plane [18], as shown in Figure 1(a). Recently, Sun et al. suggested that part of the conduction band minimum (CBM) originates from the covalence-like bonding state of $Mg_1$ 3s orbital and $Mg_2$ 3s orbital and there was also a small amount of antibonding-like interaction between $Mg_1$ 3s and Sb 5s orbitals, where $Mg_1$ represents the Mg at the Sb-octahedral center (0, 0, 0) while $Mg_2$ is the Mg at the tetrahedral center (0.3333, 0.6667, 0.3718(4)) [29]. Figure 1(b) shows the charge density in (011) plane of the trigonal $Mg_3Sb_2$. Detailed analysis of the band composition near CBM shows that the states near CBM consist of $Mg_1$ 3s orbitals, $Mg_2$ 3s orbitals, and Sb 5s orbitals. The most weighted contribution to conductive network comes from the dispersive $Mg_1$ 3s orbitals. Furthermore, our first-principles calculations also suggest that an increase of $Mg_1$-$Mg_2$ distance reduces the overlap of $Mg_1$ 3s and $Mg_2$ 3s orbitals that constitute the $Mg_1$-$Mg_2$ "bond." As the distance between $Mg_1$ and $Mg_2$ increases with strain, the difference of the squared wave function, between pristine and the one with 4% strain, shows that (i) the overlap of $Mg_1$ 3s and $Mg_2$ 3s orbitals at CBM reduces and (ii) the released charge would go to $Mg_1$ 3s orbitals and enhance the antibonding between $Mg_1$ 3s orbitals that is the most pronounced constituent around CBM (see Figure 1(c)). Therefore, it leads to a more dispersive band (i.e., lighter band) (see Figure 1(d)). The red line with solid circles in Figure 1(d) plots the DOS effective mass of conduction band minimum of $Mg_3Sb_2$ as a function of the strain along the $c$-axis. An almost linear decline in the band effective mass is observed when the strain increases from 1% to 4%. When acoustic phonon scattering is considered as the dominant scattering mechanism, the maximum power factor is proportional to the ratio $N_v/m^*$ (the derivation is given in SI A). A smaller effective mass (lighter band)

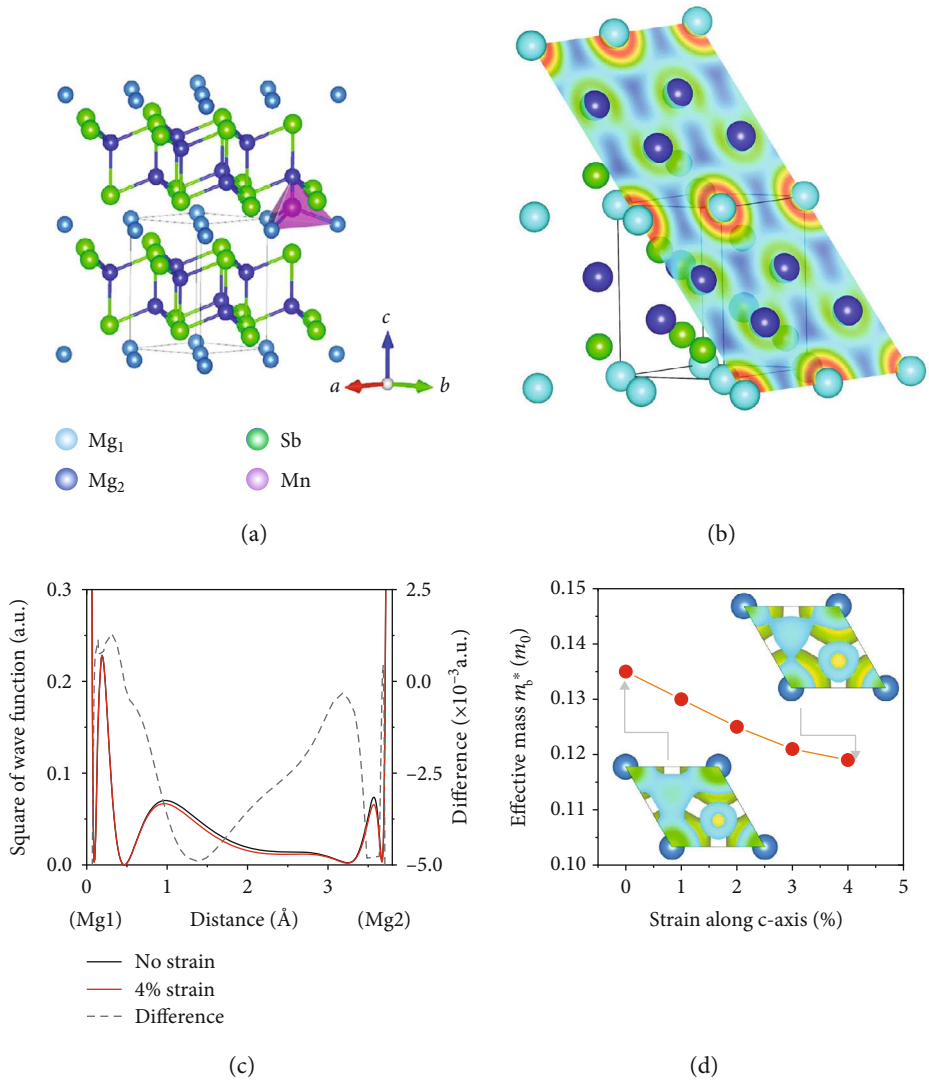


FIGURE 1: (a) Crystalline structure of $Mg_3Sb_2$ with Mn at the interstitial site. (b) Charge density in (011) plane. (c) The square of real-space wave function (i.e., the "charge" density) at CBM along $Mg_1$-$Mg_2$ line for $Mg_3Sb_2$ bulk (black solid line), under 4% strain (red solid line) along the *c*-axis and the difference (black dotted line) between "charge" density of $Mg_3Sb_2$ under 4% strain and bulk. Clear reduction of the covalence-like overlap of $Mg_1$ and $Mg_2$ 3s orbitals between $Mg_1$ and $Mg_2$ is shown with the strain and the released "charge" mostly goes to $Mg_1$. (d) Strain-dependent effective mass at conduction band edge. The inset compares the calculated charge density distribution of the two cases in the a-b cross section at the *c*-axis fractional coordinate $z = 0.18$, with the same setting of isosurface around 15% of the maximum values.

corresponds to the higher carrier mobility and the increased power factor [27, 30, 31]. Li et al. also suggested an enhanced power factor of $Mg_3SbBi$ as a biaxial strain was used in their first-principles calculation [28].

Figure 2 provides more information on the relation between carrier effective mass of $Mg_3Sb_2$ and $Mg_1$-$Mg_2$ distance according to our first-principles calculations. Experimentally, partial substitution of Sb atoms with Bi atoms expands the crystalline lattice, as shown in Figure 2(a). The XRD patterns of $Mg_3Sb_{2-y}Bi_y$ ($y = 1.0$~$2.0$) powders (grinded by SPS bulks) are given in Fig. S1 (SI). All the samples show a single phase with a $La_2O_3$-type trigonal structure. The lattice parameters and distance of $Mg_1$-$Mg_2$ are derived from the Rietveld refinement. An almost linear expansion is observed that the lattice parameter *c* varies from 7.296 Å to 7.416 Å (Fig. S2, SI) with increasing Bi content, indicating a complete solid solution of $Mg_3Sb_2$ and $Mg_3Bi_2$, and the *c*/*a* ratio remained around 1.587, which is close to that of pure $Mg_3Sb_2$. As a result, the $Mg_1$-$Mg_2$ distance increases from 3.832 Å to 3.891 Å as the Bi content increases from $y = 1.0$ to $y = 2.0$. The estimated $Mg_1$-$Mg_2$ distances in $Mg_3Sb_2$ and $Mg_3Sb_{1.5}Bi_{0.5}$ are 3.761 Å and 3.786 Å, respectively. Figure 2(b) plots the effective mass for the single band ($m_b^*$) as a function of $Mg_1$-$Mg_2$ distance. Here, both the *c*-axis strain and Bi alloying effect increase the $Mg_1$-$Mg_2$ distance. The DOS effective mass at the conduction band edge decreases with increasing $Mg_1$-$Mg_2$ distance. Bi alloying increases the

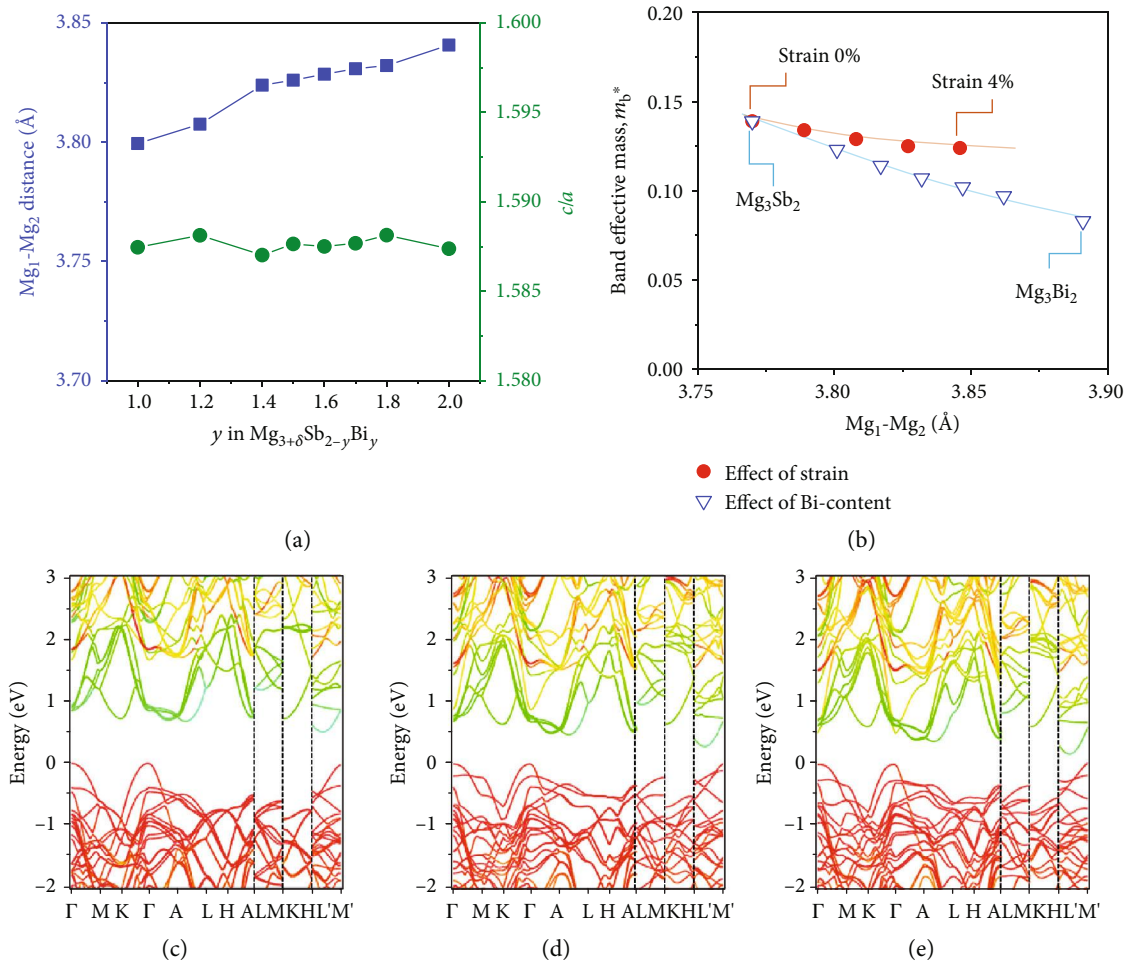


FIGURE 2: (a) $Mg_1$-$Mg_2$ distance and the ratio $c/a$ as function of Bi content. (b) Band effective mass $m_b$ as a function of the local distance of $Mg_1$-$Mg_2$ for the case with the $c$-axis strain and Bi alloying effect. (c–e) Calculated band structures for $Mg_3Sb_{2-y}Bi_y$ solid solutions with (c) $y = 0.0$, (d) $y = 1.0$, and (e) $y = 1.5$. In each figure, the color indicates the weight values (green: 1.0; red: 0.0) of Mg 3s orbitals in the band structures. The bands near CBM are mainly from Mg 3s orbitals.

distance between $Mg_1$ and $Mg_2$ and weakens the covalence-like bonding between $Mg_1$ 3s and $Mg_2$ 3s orbitals. However, the slopes of the two curves, as shown in Figure 2(b), are slightly different. The change in band effective mass mb* from Bi alloying is more complicated because (1) adding Bi into the system expands the lattice not only along the $c$-axis but also in the a-b plane (Fig. S2, SI) and (2) adding Bi leads to the upward shifting of valence bands and the narrowing of band gaps. The upward shifting of valence bands brings hybridization between Bi p orbitals from valence bands and $Mg_1$ 3s orbitals from conduction bands. Such hybridization makes bands more dispersive, therefore lighter effective mass. A similar tensile strain-dependent reduction of band DOS effective mass was also reported in the typical semiconductor with well-known covalent bonds, such as Ge [32] and Si [33].

A closing band gap of $Mg_3Sb_{2-y}Bi_y$ with increasing Bi content has been theoretically predicted by many researchers [27, 34]. Our previous experiments also proved this [4]. Zhang et al. suggested a transition from semiconductor to semimetal as the Bi content increases and goes higher than $y = 1.5$ ($Mg_3Sb_{2-y}Bi_y$) [34]. However, in our calculation, the band gap remains as large as 0.17 eV for the sample $Mg_3Sb_{0.5}Bi_{1.5}$ without spin-orbit correction. Our calculations for the $Mg_3Sb_{2-y}Bi_y$ ($y = 0$, 0.5, 0.75, 1, 1.25, 1.5, and 2.0) family give the same trend as shown in Figures 2(c)–2(e) and Table 1. The narrowing of the band gap with increasing Bi concentration is attributed to the upward shift of valence band maximum since the valence band maximum mainly consists of Sb and Bi p orbitals, and Bi p orbitals are more dispersive and lie at higher energy levels than Sb p orbitals. The band shape at CBM does not change much within the calculated Sb/Bi ratio window, but the effective mass at CBM decreases monotonically. Furthermore, the color indicator also shows that all the $Mg_3Sb_{2-y}Bi_y$ family members have a similar CBM between M* and L*, mainly raised from the Mg3s orbital. This suggests that the alloying disordering at the Sb site might have less impact on the transport of the electron since its transport channel in the real space is around the Mg site.

Figure 3 shows the Hall measurement of the as-fabricated $Mg_{3+\delta}Sb_{2-y}Bi_y$, together with reported theoretical

Table 1: First-principles calculation for $Mg_3Sb_{2-y}Bi_y$.

| $y$ | Band gap at $\Gamma$-CBM (eV) | Band gap at $\Gamma$-K (eV) | Effective mass at CBM ($m_0$) | Lattice constant $a$ (Å) | Lattice constant $c$ (Å) | $Mg_1$-$Mg_2$ distance (Å) |
|---|---|---|---|---|---|---|
| 0.00 | 0.50 | 0.72 | 0.139 | 4.596 | 7.276 | 3.770 |
| 0.50 | 0.39 | 0.68 | 0.123 | 4.625 | 7.324 | 3.801 |
| 0.75 | 0.33 | 0.66 | 0.114 | 4.639 | 7.344 | 3.817 |
| 1.00 | 0.28 | 0.64 | 0.107 | 4.644 | 7.363 | 3.832 |
| 1.25 | 0.22 | 0.62 | 0.102 | 4.664 | 7.387 | 3.847 |
| 1.50 | 0.17 | 0.61 | 0.097 | 4.681 | 7.409 | 3.862 |
| 2.00 | 0.14 | 0.58 | 0.083 | 4.718 | 7.453 | 3.891 |

and experimental data from literature. The carrier concentrations of as-fabricated $Mg_{3+\delta}Sb_{2-y}Bi_y$ samples show a weak dependence on Bi content in the range of $y = 1.0$-1.6, with an average Hall carrier concentration of ~$4 \times 10^{19}$ $cm^{-3}$, as shown in Figure 3(a). For the composition of $Mg_{3+\delta}Sb_{1.5}Bi_{0.5}$ with 1% Te and 1% Mn, our measured Hall carrier concentration ($3.52 \times 10^{19}$ $cm^{-3}$) is slightly higher than the reported data [8, 27, 35]. The effective charge carrier per Te was estimated to be 0.30, 0.47, and 0.56 electron/atom as Bi content is $y = 0$, 0.5, and 1.0, respectively. Then, it reached a saturated value of about 0.55 electron/atom when Bi content gets larger than $y = 1.0$, which indicates that Te is a strong donor in $Mg_{3+\delta}Sb_{2-y}Bi_y$ that is comparable with Te in $CoSb_{3-x}Te_x$ (0.4 electron/atom) [36]. Figure 3(b) shows that the Hall mobility of as-fabricated $Mg_{3+\delta}Sb_{2-y}Bi_y$ increases from 48.0 to 68.8, 169.8, 195.9, 201.8, 247.0, and 247.3 $cm^2 V^{-1} s^{-1}$ as the Bi content increases from $y = 0$ to 0.5, 1, 1.2, 1.4, 1.5, and 1.6, respectively. Based on our measured data together with theoretical and experimental ones from literature, a weak alloying effect was found [4, 5, 7, 8, 18, 35, 37–40], suggesting that the disordering Sb/Bi has a weak coupling effect on the charge transport channel. The Pisarenko curve was also used to analyze the alloying effect (Fig. S3, SI). The charge carrier effective masses were derived from an equivalent single band mode and changed from 1.15 to 1.05, 0.89, 0.89, 0.91, and 0.86 $m_0$ as the Bi content increased from $y =$ 0.5 to 1, 1.2, 1.4, 1.5, and 1.6. It is noted that the theoretical carrier effective mass, derived from $m^* = N_v^{2/3} m_b^*$, is less than the experimental observed value, where $N_v$ and $m_b^*$ are the degeneration number of the CBM and band effective mass (Figures 1(d) and 2(b)). The extra disagreement between first-principles calculations and experiments could be related to the adaption of theoretical lattice constants at zero Kelvin and the screened hybrid functional HSE06. Furthermore, the conduction network forms a protected electron transport channel, away from the disordering Sb/Bi. Due to the combined effect of the electronic transport channel protection and the increased $Mg_1$-$Mg_2$ distance, a high Hall mobility of ~247 $cm^2 V^{-1} s^{-1}$ is obtained in $Mg_{3+\delta}Sb_{0.5}Bi_{1.5}$ and $Mg_{3+\delta}Sb_{0.4}Bi_{1.6}$ with 1% Te and 1% Mn samples, much higher than that of the conventional composition $Mg_{3+\delta}Sb_{1.5}Bi_{0.5}$, as shown in Figure 3(c) [36, 38–40]. Figure 3(d) shows the weighted mobility $U = (m^*)^{3/2}\mu$ calculated by the carrier effective mass using the equivalent single band model and carrier mobility by Hall measurement. The weighted mobility increases from 85.5 to 183.7, 163.8, 169.7, 217.6, and 195.9 $cm^2 V^{-1} s^{-1}$ as the Bi content increases from $y = 0.5$ to $y = 1.0$, 1.2, 1.4, 1.5, and 1.6, respectively. This trend is consistent with our theoretical interpretation of the increasing $Mg_1$-$Mg_2$ distance and decreasing DOS-$m^*$ at CBM.

Figure 4 shows the temperature-dependent electrical transport properties of as-fabricated $Mg_{3+\delta}Sb_{2-y}Bi_y$ ($y = 1.0$-2.0) with 1% Te and 1% Mn. The data of our previously reported $Mg_{3+\delta}Sb_{1.5}Bi_{0.5}$ is also shown for comparison [4]. Firstly, a positive correlation between temperature and electrical resistivity is found in all samples without notable abnormal negative $d\rho/dT$ near room temperature. It should be resulted from suppressed formation of Mg vacancy by using excess Mg [22] and interstitial Mn [4] and less grain boundary scattering [21] due to a large grain size of 5-10 $\mu$m and high carrier concentration. The SEM images of the fracture section of as-fabricated $Mg_{3+\delta}Sb_{2-y}Bi_y$ samples are shown in Fig. S4, indicating a grain size of 5-10 $\mu$m. Secondly, due to the nearly unchanged carrier concentration and increasing carrier mobility with increasing Bi/Sb ratio, the room temperature electrical resistivity decreases from 8.8 to 8.2, 7.6, 6.0, 6.7, 6.2, 5.7, and 5.0 $\mu\Omega$m as the content of Bi increases from $y = 1.0$ to $y = 1.2$, 1.4, 1.5, 1.6, 1.7, 1.8, and 2.0, respectively (Figure 4(a)). It is noted that the $Mg_{3+\delta}Sb_{0.5}Bi_{1.5}$ sample has a low electric resistivity that is only half of that of the previously reported $Mg_{3+\delta}Sb_{1.5}Bi_{0.5}$ because of its high carrier mobility. Furthermore, the room temperature Seebeck coefficient of $Mg_{3+\delta}Sb_{2-y}Bi_y$ ($y = 1.0$-1.7) shows a weak Bi/Sb ratio dependence (staying at almost constant around 145 $\mu V K^{-1}$) which is consistent with the trend of carrier concentration. As Bi content increases from $y = 1.7$ to $y = 1.8$ and 2.0, the Seebeck starts to decrease from -145 $\mu V K^{-1}$ to -126.7 $\mu V K^{-1}$ and -81.4 $\mu V K^{-1}$, respectively, shown in Figure 4(b). Figure 4(c) plots the temperature-dependent power factor of $Mg_{3+\delta}Sb_{2-y}Bi_y$ ($y = 1.0$-2.0) calculated from the measured electrical resistivity and Seebeck coefficient. All the as-fabricated $Mg_{3+\delta}Sb_{2-y}Bi_y$ ($y = 1.0$-2.0) samples, except for $Mg_{3+\delta}Bi_2$, have a large power factor over 2500 $\mu W m^{-1} K^{-2}$ near room temperature. The largest room temperature power factor of 3470 $\mu W m^{-1} K^{-2}$ is obtained in $Mg_{3+\delta}Sb_{0.5}Bi_{1.5}$, which is 50% larger than that of our previously reported $Mg_{3+\delta}Sb_{1.5}Bi_{0.5}$ and also 17% larger than a recently reported

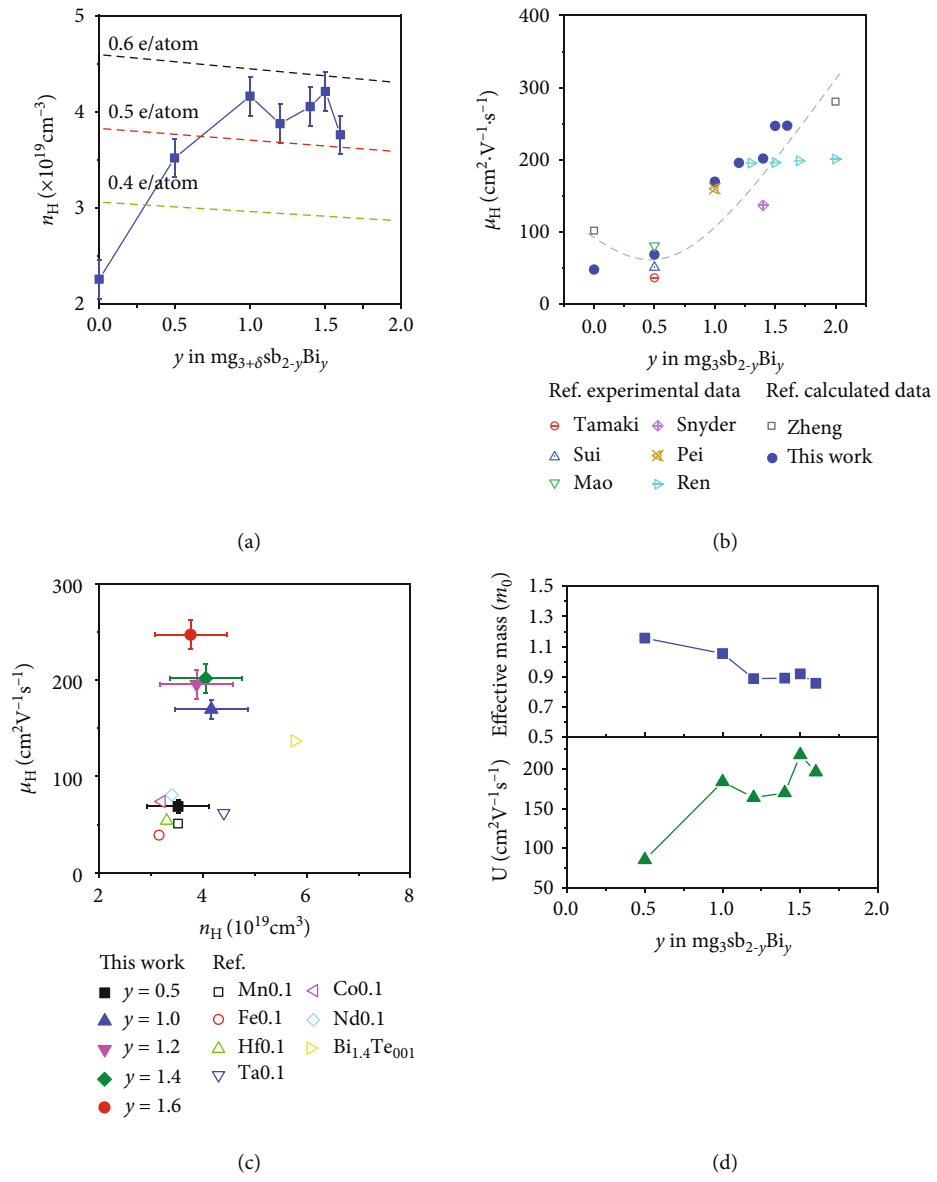


FIGURE 3: (a) Hall carrier measurement of $Mg_{3+\delta}Sb_{2-y}Bi_y$ solid solutions ($y$ = 0.5, 1, 1.2, 1.4, and 1.6). (b) Bi content-dependent Hall mobility, theoretical and experimental data from literature as references [5, 7, 8, 18, 28, 35, 39]. (c) Comparison of Hall carrier concentration and mobility in this work and reference reported $Mg_{3+\delta}Sb_{2-y}Bi_y$ system [8, 38–40]. (d) Weighted mobility and electron effective mass of $Mg_{3+\delta}Sb_{2-y}Bi_{y-0.01}Te_{0.01}$:$Mn_{0.01}$ solid solutions ($y$ = 0.5-2.0).

Bi-rich $Mg_{3+\delta}Sb_{0.6}Bi_{1.4}$ (~2960 $\mu$W m$^{-1}$ K$^{-2}$) and 26% larger than $Mg_{3.05}Sb_{2-x-y}Bi_{y-x}Te_x$ (~2750 $\mu$W m$^{-1}$ K$^{-2}$) [7, 8]. More comparisons were included in Fig. S5 (SI). Figure 4(d) plots room temperature power factor as a function of reduced Fermi level under the acoustic phonon dominant scattering (calculation details are given in SI A), suggesting that the sample $Mg_{3+\delta}Sb_{1.0}Bi_{1.0}$ was very close to the optimized carrier concentration while $Mg_{3+\delta}Sb_{2-y}Bi_y$ ($y$ = 1.2-1.8) would be overdoped. The optimized reduced Fermi energy ($E_F/k_BT$) is estimated to be around 0.67, equal to $E_F$ = 0.017 eV at room temperature, which corresponds to a Seebeck coefficient of -167 $\mu$V K$^{-1}$.

Figure 4(e) compares the average power factor of $Mg_{3+\delta}Sb_{2-y}Bi_y$ ($y$ = 1.0-2.0) in the temperature range of 50-250°C. All the samples (except $y$ = 2.0) have a value over ~3000 $\mu$W m$^{-1}$ K$^{-2}$, which is 166% higher than Tamaki's $Mg_{3+\delta}Sb_{1.5}Bi_{0.5}$ (1130 $\mu$W m$^{-1}$ K$^{-2}$) and also about 16% higher than that of previously reported $Mg_{3+\delta}Sb_{1.5}Bi_{0.5}$ (2590 $\mu$W m$^{-1}$ K$^{-2}$) [4, 18]. This has already surpassed many polycrystalline n-type $Bi_2(Te,Se)_3$, which can be comparable with textured $Bi_2(Te,Se)_3$ [41, 42] and commercially available $Bi_2(Te,Se)_3$ ingot in the temperature range of 50-250°C. A more accurate relationship between output power density and the power factor is given in equation (1); the engineering power factor (Figure 4(f)) is calculated as equation (2) [43].

$$P_{output} = (PF)_{eng}\frac{\Delta T}{L}\frac{\sqrt{1+ZT_{avg}}}{\left(1+\sqrt{1+ZT_{avg}}\right)^2}, \quad (1)$$

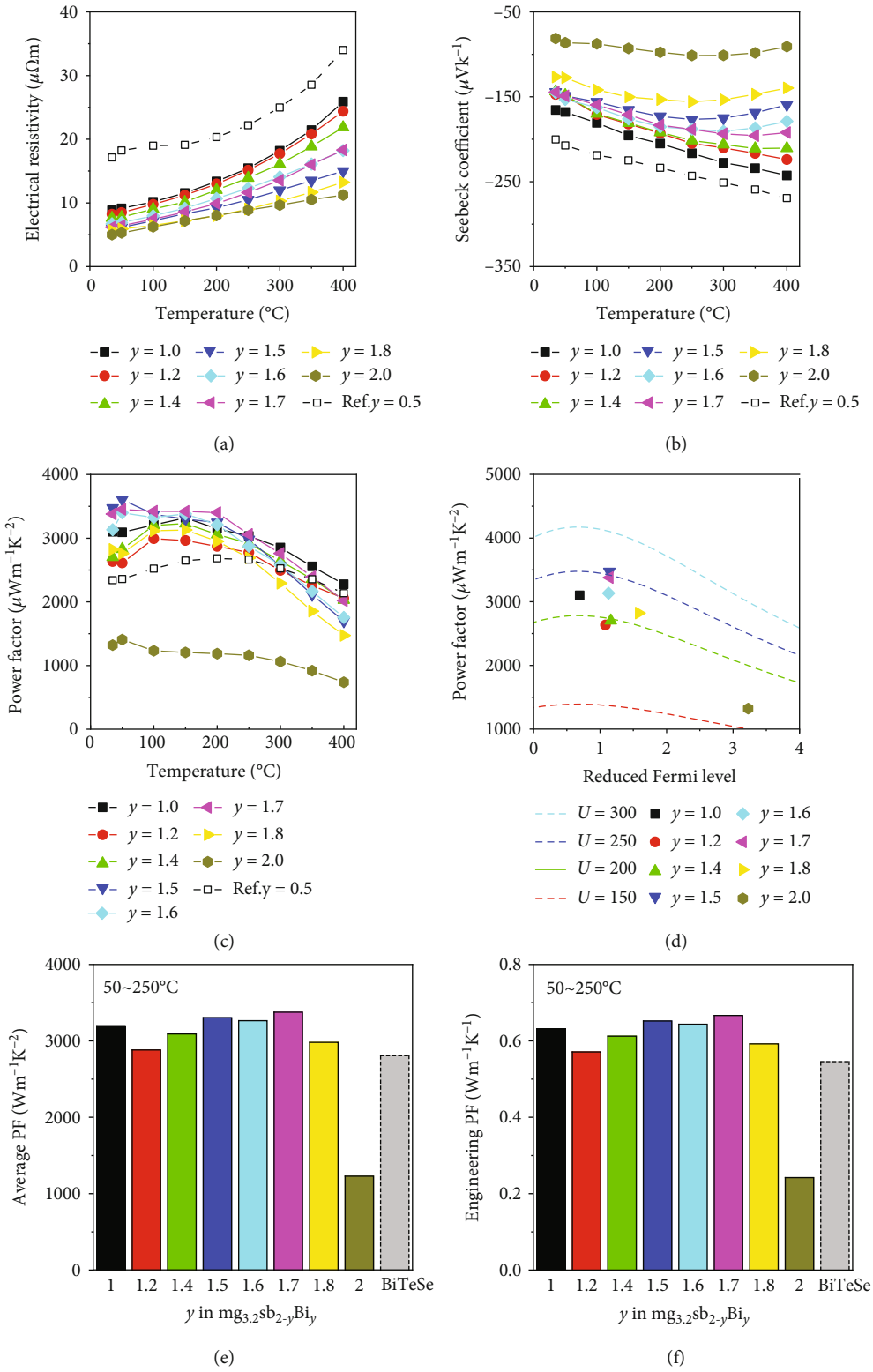


FIGURE 4: Temperature dependence of (a) electrical resistivity, (b) Seebeck coefficient, and (c) power factor of $Mg_{3+\delta}Sb_{2-y}Bi_y$ ($y$ = 1.0, 1.2, 1.4, 1.5, 1.6, 1.7, 1.8, and 2.0), previous $y$ = 0.5 as reference [4]. (d) Power factor as a function of reduced Fermi level at room temperature in condition of different weighted mobility. (e) Average power factor and (f) engineering power factor in the temperature range of 50-250°C, with $Bi_2Te_{2.3}Se_{0.7}$ as a reference [41].

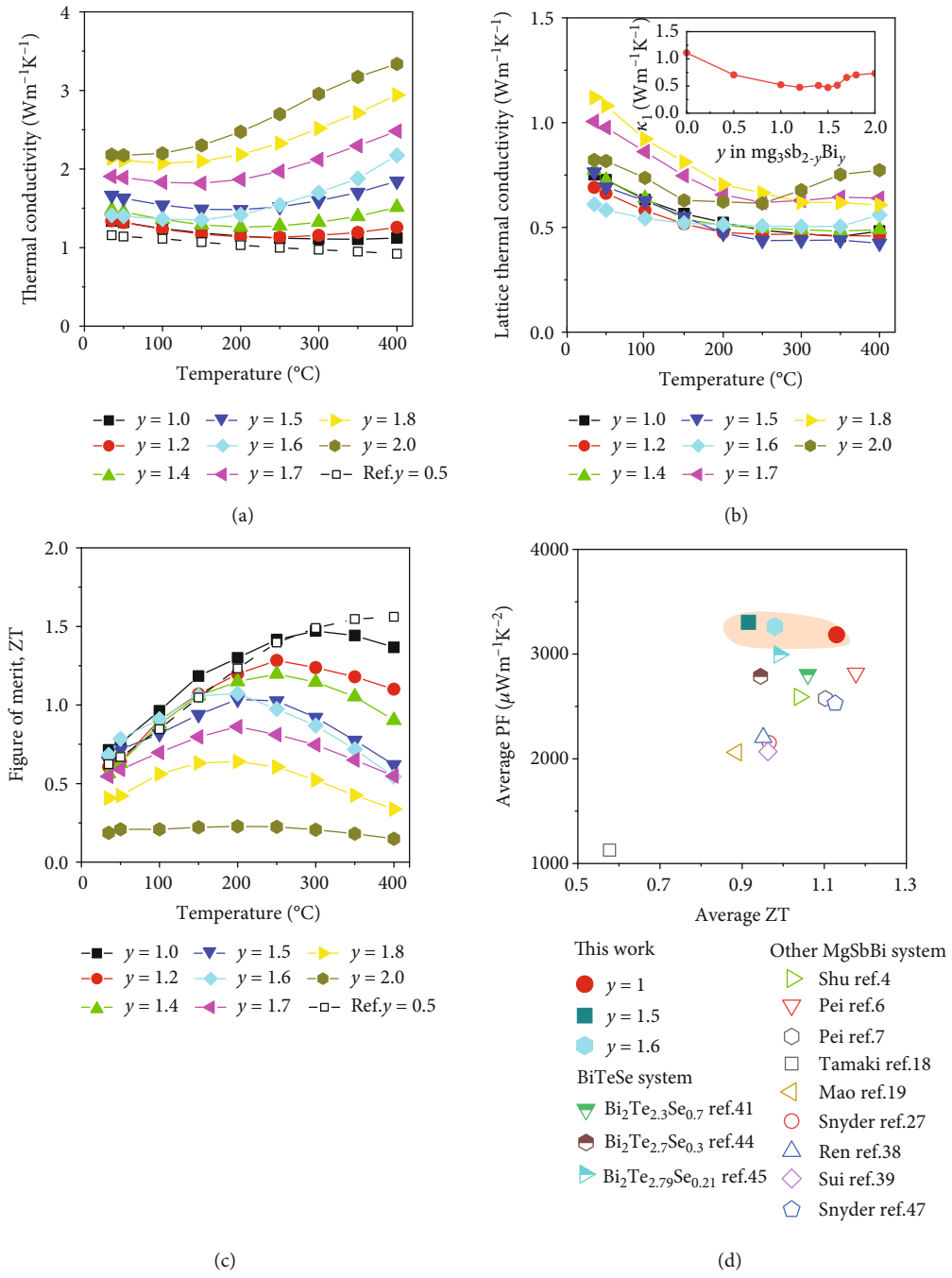


FIGURE 5: Temperature dependence of (a) thermal conductivity, (b) lattice thermal conductivity (the inset is lattice thermal conductivity as a function of Bi content at 200°C), and (c) figure of merit ZT of $Mg_{3+\delta}Sb_{2-y}Bi_y$ ($y$ = 1.0, 1.2, 1.4, 1.5, 1.6, 1.7, 1.8, and 2.0), previously reported $y$ = 0.5 as reference [4, 18]. (d) Synergistic improvement of average ZT and average power factor of $Mg_{3+\delta}Sb_{2-y}Bi_{y-0.01}Te_{0.01}$:$Mn_{0.01}$ solid solutions in the temperature range of 50-250°C, compared with literature reported $Mg_{3+\delta}Sb_{2-y}Bi_y$ and $Bi_2$ (Te, Se)$_3$ as reference.

$$(\mathrm{PF})_{\mathrm{eng}} = \frac{\left(\int_{T_c}^{T_h} S(T)dT\right)^2}{\int_{T_c}^{T_h} \rho(T)dT}, \quad (2)$$

where $\Delta T$ is the temperature difference, $L$ is the TE-leg length, and $S(T)$ and $\rho(T)$ are temperature-dependent Seebeck coefficient and electrical resistivity. In the temperature range of 50-250°C, all the samples (except $y$ = 2.0) have an engineering power factor of about 0.6 W m$^{-1}$ K$^{-1}$, which is 100% larger than Tamaki's $Mg_{3+\delta}Sb_{1.5}Bi_{0.5}$ (0.3 W m$^{-1}$ K$^{-1}$) and also 20% larger than that of previously reported $Mg_{3+\delta}Sb_{1.5}Bi_{0.5}$ (0.5 W m$^{-1}$ K$^{-1}$) [4, 18].

Figures 5(a) and 5(b) show the temperature-dependent thermal properties of $Mg_{3+\delta}Sb_{2-y}Bi_y$ ($y$ = 1.0-2.0). At room temperature, the thermal conductivity increases from 1.31 to 1.34, 1.47, 1.64, 1.41, 1.90, 2.13, and 2.18 W m$^{-1}$ K$^{-2}$, as the Bi content increases from $y$ = 1.0 to 1.2, 1.4, 1.5, 1.6,

1.7, 1.8, and 2.0, respectively. A notable bipolar effect is observed in all the samples which are characterized by an increasing thermal conductivity with temperature at the high temperature end. Furthermore, the samples with more Bi (i.e., larger $y$ value in the formula of $Mg_{3+\delta}Sb_{2-y}Bi_y$) have a lower starting temperature, which is consistent with narrowing band gap predicated by our theoretical calculations. The lattice thermal conductivity is estimated by subtracting the contribution of electronic part ($\kappa_{ele}$) and bipolar part ($\kappa_{bip}$) from the total thermal conductivity ($\kappa_{tot}$), i.e., $\kappa_{lat} = \kappa_{tot} - \kappa_{ele} - \kappa_{bip}$ (Figure 5(b)). The details of the calculation relative to the electronic thermal conductivity ($\kappa_{ele}$) and bipolar thermal conductivity ($\kappa_{bip}$) are given in SI B. At room temperature, $\kappa_{lat}$ changes from 0.75 to 0.69, 0.77, 0.76, 0.61, 1.00, 1.12, and 0.82 $W m^{-1} K^{-2}$ as the Bi content increases from $y = 1.0$ to 1.2, 1.4, 1.5, 1.6, 1.7, 1.8, and 2.0, respectively. For comparison, $\kappa_{lat}$ of $Mg_3Sb_2$ and $Mg_3Sb_{1.5}Bi_{0.5}$ from our previous work are estimated to be 1.46 $W m^{-1} K^{-2}$ and 0.73 $W m^{-1} K^{-2}$ [4]. $\kappa_{lat}$ of $Mg_{3+\delta}Sb_{1.0}Bi_{1.0}$ is 48% lower than that of $Mg_3Sb_2$ and 12% lower than that of $Mg_3Bi_2$. This decrease in lattice thermal conductivity is the result of alloying scattering on the transport of the phonon.

Figure 5(c) compares ZT as a function of temperature of $Mg_{3+\delta}Sb_{2-y}Bi_y$ ($y = 1.0$-2.0). $Mg_{3+\delta}Sb_{1.0}Bi_{1.0}$ shows a peak ZT of 1.5 at 300°C, while a room temperature ZT of 0.75, which is 275% higher than that of Tamaki's $Mg_{3+\delta}Sb_{1.5}Bi_{0.5}$ ($ZT_{@RT} = 0.2$) and 20% higher than that of our previously reported $Mg_{3+\delta}Sb_{1.5}Bi_{0.5}$ ($ZT_{@RT} = 0.62$), as shown in Figure 5(c) [4, 18]. This is also comparable with recently reported $Mg_{3.2}Bi_{1.998-x}Sb_xTe_{0.002}$ at room temperature [5] and higher than $Mg_{3+\delta}Sb_{0.6}Bi_{1.4}$, which behaves $ZT_{@RT}$~0.68 and peak ZT of ~1.1 [8]. It is comparable with those of commercially available n-type $Bi_2Te_3$ ingot ($ZT_{@RT} = 0.71$) [4]. Moreover, in the temperature range of 50-250°C, $Mg_{3+\delta}Sb_{1.0}Bi_{1.0}$ has an engineering ZT of 0.56, which is 16.7% higher than our previously reported $Mg_{3+\delta}Sb_{1.5}Bi_{0.5}$ ($(ZT)_{eng} = 0.48$) and $Bi_2Te_{3-x}Se_x$ ($(ZT)_{eng} = 0.47$) (data from literatures are plotted on Fig. S7, SI) [4, 44]. Furthermore, the thermoelectric properties of three batches of $Mg_{3+\delta}Sb_{1.0}Bi_{1.0}$ and circling electrical property test for one of the samples were given in Fig. S6 (SI), which shows that the results are repeatable. Finally, a dual parameter criteria of "ZT versus PF" [43] are used to select the better thermoelectric materials with a consideration for requirements of efficiency and power density at the same time [45]. Figure 5(d) clearly suggests that $Mg_{3+\delta}Sb_{1.0}Bi_{1.0}$ in this work surpasses any other $Mg_{3+\delta}Sb_{2-y}Bi_y$ material in this work and the $Bi_2Te_{3-x}Se_x$ family [4, 6, 7, 18, 19, 27, 38, 39, 41, 44, 46, 47], for its high average ZT of 1.13 and an average power factor of 3184 $\mu W m^{-1} K^{-2}$. (Reference data from literature is plotted on Fig. S8, SI.).

## 3. Conclusion

We have successfully enhanced the room temperature thermoelectric performance of $Mg_{3+\delta}Sb_{2-y}Bi_y$ by the strategy of electronic transport channel protection and tuning in real space. It was found that the increased carrier mobility was closely related to the weakening covalence-like bonding between $Mg_1$ 3s and $Mg_2$ 3s orbitals and hence the lightening DOS effective mass. Experimentally, our $Mg_{3+\delta}Sb_{0.5}Bi_{1.5}$ samples reached a high carrier mobility of 247 $cm^2 V^{-1} s^{-1}$ and high power of 3470 $\mu W m^{-1} K^{-2}$ at room temperature. We also suggest that, in a dual parameter criteria of "ZT versus PF," $Mg_{3+\delta}Sb_{1.0}Bi_{1.0}$ would be a promising room temperature thermoelectric material, to replace the classic n-type $Bi_2Te_{2.7}Se_{0.3}$, for its high values of $ZT_{@RT} = 0.75$, $PF_{@RT} = 3100\ \mu W m^{-1} K^{-2}$ at room temperature, $(ZT)_{avg} = 1.13$, and $(PF)_{avg} = 3184\ \mu W m^{-1} K^{-2}$ in the temperature range of 50-250°C, which gives an efficiency of 8.5% under ideal adiabatic condition. Furthermore, the electronic transport channel protection and tuning in real space could be a new electronic engineering strategy to increase the carrier mobility.

## 4. Experimental Procedures

*4.1. Sample Synthesis.* The samples with nominal compositions of $Mg_{3+\delta}Sb_{2-y}Bi_{y-0.01}Te_{0.01}$:$Mn_{0.01}$ were synthesized by mechanical alloying and spark plasma sintering (SPS). High-purity magnesium turnings (Mg, >99.9%; Acros Organics), antimony shots (Sb, 99.999%; 5N Plus), bismuth shots (Bi, 99.999%; 5N Plus), tellurium shots (Te, 99.999%; 5N Plus), and manganese powders (Mn, 99.95%; Alfa Aesar) were weighed according to the composition of $Mg_{3+\delta}Sb_{2-y}Bi_{y-0.01}Te_{0.01}$:$Mn_{0.01}$ ($\delta = 0.2$, $y = 1.0$, 1.2, 1.4, 1.5, 1.6, 1.7, 1.8, and 2.0), simplified as $Mg_{3+\delta}Sb_{2-y}Bi_y$ in the text, and were then loaded into a stainless steel ball milling jar together with stainless steel balls in a glove box in an argon atmosphere with the oxygen level < 1 ppm. After ball milling for 8 hours in SPEX 8000D, or 8000 M, the ball-milled powders were loaded into a graphite die with an inner diameter of 15 mm in a glove box. Graphite die with loading powder was immediately sintered at 675°C under a pressure of 50 MPa for 5 min in SPS division (SPS-211Lx, Fuji Electronic Industrial Co. LTD). The SPS bulks are ~15 mm in diameter and ~8 mm in thickness. The Seebeck coefficient, electrical resistivity, and thermal diffusivity were measured in the directions perpendicular to pressure.

*4.2. Thermoelectric Characterization.* Electrical properties, including Seebeck coefficient, electrical resistivity, and power factor, were measured by ZEM-3, ULVAC Riko, under a 0.01 MPa pressure helium atmosphere from RT to 400°C. Measured samples were cut into about 2.5 mm × 3 mm × 13 mm pieces. Thermal conductivity was calculated by equation $\kappa = DC_p\rho$, where $D$ is thermal diffusivity measured by laser flash method (LFA 467; Netzsch) using about 6 mm × 6 mm × 1 mm pieces, $d$ is density measured by the Archimedean method, and specific heat ($C_p$) is tested by differential scanning calorimetry (Discovery DSC, Waters LLC), shown in Fig. S9 (SI).

*4.2.1. Hall Effect Measurement.* Hall coefficient was measured by Physical Property Measurement System (PPMS-14L, Quantum Design) with four-point method in magnetic field from -5 T to 5 T. Tested samples were cut into about

6 mm × 6 mm × 1 mm pieces and then soldered to Φ0.1 mm enameled wire with In as the solder. Hall carrier concentration was calculated by $n_H = 1/|R_H|e$, and Hall mobility was calculated by $\mu_H = |R_H|/\rho$, where $e$ is elementary charge and $\rho$ is measured electrical resistivity.

*4.3. X-Ray Diffraction.* SPS bulks were grinded into powder in a glove box, and then, the phase composition was characterized by X-ray diffraction (Rigaku SmartLab) with Cu $K_\alpha$ radiation ($\lambda = 1.54$ Å, operating at 40 kV/15 mA with $K_\beta$ foil filter). XRD patterns were further refined by the Rietveld method to calculate lattice parameter and $Mg_1$-$Mg_2$ distance.

*4.4. Calculation Methods.* The first-principles calculations are based on density functional theory (DFT) [48, 49] and the screened hybrid functional HSE06 [50, 51] as implemented in the Vienna Ab Initio Simulation Package (VASP) code [52]. Projected augmented wave (PAW) potentials [53] with plane-wave basis set and an energy cutoff of 550 eV are used. The valence electronic configurations for Mg, Sb, and Bi are $3s^2$, $5s^25p^3$, and $6s^26p^3$ in the pseudopotentials, respectively. For integrations over the Brillouin zone, we use 5 × 5 × 3 Monkhorst-Pack k-point mesh [54] for 40-atom cells (2 × 2 × 2). The atomic positions are fully relaxed until the forces on each atom are less than 0.005 eV/Å and total energy differences between two consecutive steps are less than $10^{-6}$ eV. The lowest-energy structural configurations for alloy systems are constructed by Supercell program [55] and direct energy comparison.

## Conflicts of Interest

There are no conflicts to declare.

## Authors' Contributions

W.S. Liu and Z.J. Han designed the experiment; Z.J. Han conducted the synthesis and TE transport property measurement; Z.G. Gui contributed to the first-principles calculation; P. Qin and Y.B. Zhu conducted the Hall measurement; Z.J. Han and Z.G. Gui complete the writing of the manuscript; B.P. Zhang, W.Q. Zhang, L. Huang, and W.S. Liu were responsible for the interpretation of the results and revision of the manuscript. All authors discussed the results and gave comments regarding the manuscript. Z.J. Han and Z.G. Gui have equivalent contribution.

## Acknowledgments

The authors would like to thank the support of State's Key Project of Research and Development Plan No. 2018YFB0703600, NSFC Program No. 51872133, Guangdong Innovative and Entrepreneurial Research Team Program No. 2016ZT06G587, and Shenzhen Basic Research Fund under Grant Nos. JCYJ20170817105132549 and JCYJ20180504165817769. The authors would also like to thank the support of Centers for Mechanical Engineering Research and Education at MIT and SUSTech. The computing time was supported by the Center for Computational Science and Engineering of SUSTech. The authors would like to thank Prof. Gang Chen and Qian Xu of the Department of Mechanical Engineering, MIT, and Prof. Hongtao He, Prof. Liusuo Wu, and Liang Zhou, of the Department of Physics, SUSTech.

## Supplementary Materials

Fig. S1: XRD patterns of the $Mg_{3+\delta}Sb_{2-y}Bi_y$ ($y$ = 1.0, 1.2, 1.4, 1.5, 1.6, 1.7, 1.8, and 2.0) solid solution powder. Fig. S2: lattice parameter $a$ and $c$ of $Mg_{3+\delta}Sb_{2-y}Bi_y$ as function of Bi content, and dash lines show Vegard's law between $Mg_3Sb_2$ and $Mg_3Bi_2$. Fig. S3: Pisarenko's plot for $Mg_{3+\delta}Sb_{2-y}Bi_y$. It shows a decrease effective mass with higher Bi content. Fig. S4: SEM images of the fractured surface of $Mg_{3+\delta}Sb_{2-y}Bi_y$: (a) $y$ = 1.0, (b) $y$ = 1.2, (c) $y$ = 1.4, (d) $y$ = 1.5, and (e) $y$ = 1.6. Fig. S5: comparison of power factor of the $Mg_3(Sb, Bi)_2$ system [1–18]. Fig. S6: reproducibility and circling test of as-fabricated $Mg_{3+\delta}Sb_{1.0}Bi_{0.99}Te_{0.01}$:$Mn_{0.01}$. Fig. S7: temperature dependence of (a) power factor and (b) ZT of as-fabricated $Mg_{3+\delta}Sb_{2-y}Bi_y$ and $Bi_2(Te,Se)_3$ from references [8, 9, 12, 15, 17–23]. Fig. S8: engineering ZT of $Mg_{3+\delta}Sb_{2-y}Bi_{y-0.01}Te_{0.01}$:$Mn_{0.01}$ in the temperature range of 50-250°C. Fig. S9: specific heat of the $Mg_{3+\delta}Sb_{2-y}Bi_{y-0.01}Te_{0.01}$:$Mn_{0.01}$ solid solution powder. *(Supplementary Materials)*

## References

[1] W. Liu, X. Yan, G. Chen, and Z. Ren, "Recent advances in thermoelectric nanocomposites," *Nano Energy*, vol. 1, no. 1, pp. 42–56, 2012.

[2] T. Zhu, L. Hu, X. Zhao, and J. He, "New insights into intrinsic point defects in $V_2V_{I3}$ Thermoelectric materials," *Advanced Science*, vol. 3, no. 7, article 1600004, 2016.

[3] L.-D. Zhao, B.-P. Zhang, J.-F. Li, M. Zhou, W.-S. Liu, and J. Liu, "Thermoelectric and mechanical properties of nano-SiC-dispersed $Bi_2Te_3$ fabricated by mechanical alloying and spark plasma sintering," *Journal of Alloys and Compounds*, vol. 455, no. 1-2, pp. 259–264, 2008.

[4] R. Shu, Y. Zhou, Q. Wang et al., "$Mg_{3+\delta}Sb_xBi_{2-x}$ Family: a promising substitute for the state-of-the-art n-type thermoelectric materials near room temperature," *Advanced Functional Materials*, vol. 29, no. 4, article 1807235, 2019.

[5] J. Mao, H. Zhu, Z. Ding et al., "High thermoelectric cooling performance of n-type $Mg_3Bi_2$-based materials," *Science*, vol. 365, no. 6452, pp. 495–498, 2019.

[6] X. Shi, C. Sun, X. Zhang et al., "Efficient Sc-doped $Mg_{3.05-x}Sc_xSbBi$ thermoelectrics near room temperature," *Chemistry of Materials*, vol. 31, no. 21, pp. 8987–8994, 2019.

[7] X. Shi, T. Zhao, X. Zhang et al., "Extraordinary n-type $Mg_3SbBi$ thermoelectrics enabled by yttrium doping," *Advanced Materials*, vol. 31, no. 36, article 1903387, 2019.

[8] K. Imasato, S. D. Kang, and G. J. Snyder, "Exceptional thermoelectric performance in $Mg_3Sb_{0.6}Bi_{1.4}$ for low-grade waste heat recovery," *Energy & Environmental Science*, vol. 12, no. 3, pp. 965–971, 2019.

[9] W. Liu, H. S. Kim, Q. Jie, and Z. Ren, "Importance of high power factor in thermoelectric materials for power generation application: a perspective," *Scripta Materialia*, vol. 111, pp. 3–9, 2016.

[10] C. Xiao, Z. Li, K. Li, P. Huang, and Y. Xie, "Decoupling interrelated parameters for designing high performance thermoelectric materials," *Accounts of Chemical Research*, vol. 47, no. 4, pp. 1287–1295, 2014.

[11] W. Liu, J. Zhou, Q. Jie et al., "New insight into the material parameter B to understand the enhanced thermoelectric performance of $Mg_2Sn_{1-x-y}Ge_xSb_y$," *Energy & Environmental Science*, vol. 9, no. 2, pp. 530–539, 2016.

[12] P. Pichanusakorn and P. Bandaru, "Nanostructured thermoelectrics," *Materials Science and Engineering: R: Reports*, vol. 67, no. 2-4, pp. 19–63, 2010.

[13] R. W. Keyes, "High-temperature thermal conductivity of insulating crystals: relationship to the melting point," *Physical Review*, vol. 115, no. 3, pp. 564–567, 1959.

[14] A. Ioffe, *Semiconductor Thermoelements and Thermoelectric Refrigeration*, Infosearch, Ltd., London, England, 1957.

[15] H. J. Goldsmid, "Recent studies of bismuth telluride and its alloys," *Journal of Applied Physics*, vol. 32, no. 10, pp. 2198–2202, 1961.

[16] T. Zhu, Y. Liu, C. Fu, J. P. Heremans, J. G. Snyder, and X. Zhao, "Compromise and synergy in high-efficiency thermoelectric materials," *Advanced Materials*, vol. 29, no. 14, article 1605884, 2017.

[17] Y. Liu, C. Fu, K. Xia et al., "Lanthanide contraction as a design factor for high-performance half-Heusler thermoelectric materials," *Advanced Materials*, vol. 30, no. 32, article 1800881, 2018.

[18] H. Tamaki, H. K. Sato, and T. Kanno, "Isotropic conduction network and defect chemistry in $Mg_{3+\delta}$ $Sb_2$-based layered Zintl compounds with high thermoelectric performance," *Advanced Materials*, vol. 28, no. 46, pp. 10182–10187, 2016.

[19] J. Mao, Y. Wu, S. Song et al., "Defect engineering for realizing high thermoelectric performance in n-type $Mg_3Sb_2$-based materials," *ACS Energy Letters*, vol. 2, no. 10, pp. 2245–2250, 2017.

[20] J. Zhang, L. Song, K. A. Borup, M. R. V. Jørgensen, and B. B. Iversen, "New insight on tuning electrical transport properties via chalcogen doping in n-type $Mg_3Sb_2$-based thermoelectric materials," *Advanced Energy Materials*, vol. 8, no. 16, article 1702776, 2018.

[21] J. J. Kuo, S. D. Kang, K. Imasato et al., "Grain boundary dominated charge transport in $Mg_3Sb_2$-based compounds," *Energy & Environmental Science*, vol. 11, no. 2, pp. 429–434, 2018.

[22] J. Shuai, B. Ge, J. Mao, S. Song, Y. Wang, and Z. Ren, "Significant role of Mg stoichiometry in designing high thermoelectric performance for $Mg_3(Sb,Bi)_2$-based n-type zintls," *Journal of the American Chemical Society*, vol. 140, no. 5, pp. 1910–1915, 2018.

[23] Y. Pei, A. D. LaLonde, H. Wang, and G. J. Snyder, "Low effective mass leading to high thermoelectric performance," *Energy & Environmental Science*, vol. 5, no. 7, pp. 7963–7969, 2012.

[24] H. Wang, X. Cao, Y. Takagiwa, and G. J. Snyder, "Higher mobility in bulk semiconductors by separating the dopants from the charge-conducting band–a case study of thermoelectric PbSe," *Materials Horizons*, vol. 2, no. 3, pp. 323–329, 2015.

[25] U. Saparamadu, J. Mao, K. Dahal et al., "The effect of charge carrier and doping site on thermoelectric properties of $Mg_2Sn_{0.75}Ge_{0.25}$," *Acta Materialia*, vol. 124, pp. 528–535, 2017.

[26] J. Yang, L. Xi, W. Qiu et al., "On the tuning of electrical and thermal transport in thermoelectrics: an integrated theory-experiment perspective," *NPJ Computational Materials*, vol. 2, no. 1, article 15015, 2016.

[27] K. Imasato, S. D. Kang, S. Ohno, and G. J. Snyder, "Band engineering in $Mg_3Sb_2$ by alloying with $Mg_3Bi_2$ for enhanced thermoelectric performance," *Materials Horizons*, vol. 5, no. 1, pp. 59–64, 2018.

[28] J. Li, S. Zhang, B. Wang et al., "Designing high-performance n-type $Mg_3Sb_2$-based thermoelectric materials through forming solid solutions and biaxial strain," *Journal of Materials Chemistry A*, vol. 6, no. 41, pp. 20454–20462, 2018.

[29] X. Sun, X. Li, J. Yang et al., "Achieving band convergence by tuning the bonding ionicity in n-type $Mg_3Sb_2$," *Journal of Computational Chemistry*, vol. 40, no. 18, pp. 1693–1700, 2019.

[30] D. M. Rowe, *Thermoelectrics Handbook: Macro to Nano*, CRC press, 2018.

[31] K. Koumoto and T. Mori, *Thermoelectric Nanomaterials*, Springer, 2015.

[32] J. Liu, X. Sun, D. Pan et al., "Tensile-strained, n-type Ge as a gain medium for monolithic laser integration on Si," *Optics Express*, vol. 15, no. 18, pp. 11272–11277, 2007.

[33] G. Sun, Y. Sun, T. Nishida, and S. E. Thompson, "Hole mobility in silicon inversion layers: stress and surface orientation," *Journal of Applied Physics*, vol. 102, no. 8, article 084501, 2007.

[34] J. Zhang, L. Song, A. Mamakhel, M. R. V. Jørgensen, and B. B. Iversen, "High-performance low-cost n-type Se-doped $Mg_3Sb_2$-based Zintl compounds for thermoelectric application," *Chemistry of Materials*, vol. 29, no. 12, pp. 5371–5383, 2017.

[35] S. Song, J. Mao, J. Shuai et al., "Study on anisotropy of n-type $Mg_3Sb_2$-based thermoelectric materials," *Applied Physics Letters*, vol. 112, no. 9, article 092103, 2018.

[36] X. Y. Li, L. D. Chen, J. F. Fan, W. B. Zhang, T. Kawahara, and T. Hirai, "Thermoelectric properties of Te-doped $CoSb_3$ by spark plasma sintering," *Journal of Applied Physics*, vol. 98, no. 8, article 083702, 2005.

[37] S. Chen, K. C. Lukas, W. Liu, C. P. Opeil, G. Chen, and Z. Ren, "Effect of Hf concentration on thermoelectric properties of nanostructured N-type half-Heusler materials $Hf_xZr_{1-x}NiSn_{0.99}Sb_{0.01}$," *Advanced Energy Materials*, vol. 3, no. 9, pp. 1210–1214, 2013.

[38] J. Mao, J. Shuai, S. Song et al., "Manipulation of ionized impurity scattering for achieving high thermoelectric performance in n-type $Mg_3Sb_2$-based materials," *Proceedings of the National Academy of Sciences of the United States of America*, vol. 114, no. 40, pp. 10548–10553, 2017.

[39] X. Chen, H. Wu, J. Cui et al., "Extraordinary thermoelectric performance in n-type manganese doped $Mg_3Sb_2$ Zintl: high band degeneracy, tuned carrier scattering mechanism and hierarchical microstructure," *Nano Energy*, vol. 52, pp. 246–255, 2018.

[40] J. Shuai, J. Mao, S. Song et al., "Tuning the carrier scattering mechanism to effectively improve the thermoelectric properties," *Energy & Environmental Science*, vol. 10, no. 3, pp. 799–807, 2017.

[41] R. Zhai, Y. Wu, T.-J. Zhu, and X.-B. Zhao, "Tunable optimum temperature range of high-performance zone melted bismuth-telluride-based solid solutions," *Crystal Growth & Design*, vol. 18, no. 8, pp. 4646–4652, 2018.

[42] H. Kontani, "General formula for the thermoelectric transport phenomena based on fermi liquid theory: thermoelectric

power, nernst coefficient, and thermal conductivity," *Physical Review B*, vol. 67, no. 1, article 014408, 2003.

[43] H. S. Kim, W. Liu, G. Chen, C.-W. Chu, and Z. Ren, "Relationship between thermoelectric figure of merit and energy conversion efficiency," *Proceedings of the National Academy of Sciences of the United States of America*, vol. 112, no. 27, pp. 8205–8210, 2015.

[44] L. Hu, H. Wu, T. Zhu et al., "Tuning multiscale microstructures to enhance thermoelectric performance of n-type Bismuth-Telluride-based solid solutions," *Advanced Energy Materials*, vol. 5, no. 17, article 1500411, 2015.

[45] W. Liu, H. S. Kim, S. Chen et al., "n-type thermoelectric material $Mg_2Sn_{0.75}Ge_{0.25}$ for high power generation," *Proceedings of the National Academy of Sciences of the United States of America*, vol. 112, no. 11, pp. 3269–3274, 2015.

[46] W. Liu, K. C. Lukas, K. McEnaney et al., "Studies on the $Bi_2Te_3$–$Bi_2Se_3$–$Bi_2S_3$ system for mid-temperature thermoelectric energy conversion," *Energy & Environmental Science*, vol. 6, no. 2, pp. 552–560, 2013.

[47] M. Wood, J. J. Kuo, K. Imasato, and G. J. Snyder, "Improvement of low-temperature $zT$ in a $Mg_3Sb_2$–$Mg_3Bi_2$ solid solution via Mg-vapor annealing," *Advanced Materials*, vol. 31, no. 35, article 1902337, 2019.

[48] P. Hohenberg and W. Kohn, "Inhomogeneous electron gas," *Physics Review*, vol. 136, no. 3B, pp. B864–B871, 1964.

[49] W. Kohn and L. J. Sham, "Self-consistent equations including exchange and correlation effects," *Physics Review*, vol. 140, no. 4A, pp. A1133–A1138, 1965.

[50] J. Heyd, G. E. Scuseria, and M. Ernzerhof, "Hybrid functionals based on a screened Coulomb potential," *The Journal of Chemical Physics*, vol. 118, no. 18, pp. 8207–8215, 2003.

[51] A. V. Krukau, O. A. Vydrov, A. F. Izmaylov, and G. E. Scuseria, "Influence of the exchange screening parameter on the performance of screened hybrid functionals," *The Journal of Chemical Physics*, vol. 125, no. 22, article 224106, 2006.

[52] G. Kresse and J. Furthmüller, "Efficient iterative schemes for *ab initio* total-energy calculations using a plane-wave basis set," *Physical Review B*, vol. 54, no. 16, pp. 11169–11186, 1996.

[53] P. E. Blöchl, "Projector augmented-wave method," *Physical Review B*, vol. 50, no. 24, pp. 17953–17979, 1994.

[54] H. J. Monkhorst and J. D. Pack, "Special points for Brillouin-zone integrations," *Physical Review B*, vol. 13, no. 12, pp. 5188–5192, 1976.

[55] K. Okhotnikov, T. Charpentier, and S. Cadars, "Supercell program: a combinatorial structure-generation approach for the local-level modeling of atomic substitutions and partial occupancies in crystals," *Journal of Cheminformatics*, vol. 8, no. 1, p. 17, 2016.